International Journal of Modern Manufacturing Technologies
ISSN 2067–3604, Vol. XVIII, No. 1 / 2026
https://doi.org/ 10.54684/ijmmt.2026.18.1.35

# PUNCTURE RESISTANCE OF ELEMENTS WITH DIFFERENT INTERNAL STRUCTURES MADE USING 3D PRINTING TECHNOLOGY

**Paula Mąntewka[1], Andrzej Komorek[1], Robert Bąbel[1], Julia Komorek[2]**

[1]Department of Aviation, Polish Air Force University, 08-530 Deblin, Poland
[2]PRB Bruk-Bud Sp. z.o.o. 08-400 Sulbiny, Poland

Corresponding author: Andrzej Komorek, a.komorek@law.mil.pl

***Abstract:*** 3D printing is currently widely used in many areas of life. In industry, it has found its application in creating templates and prototypes. Products made using 3D printers are utilised in fields ranging from aerospace and medicine to automotive, jewellery, museum exhibits, and art. With the growing importance of 3D printing and the wide availability of fillings for creating projects, it is important to recognise the properties of printed elements. The subject of research on the puncture resistance of elements made in 3D technology is an important issue today, sporadically described in the available literature. The strength of printed products is significantly influenced by factors such as the structure of the internal filling and the value of the filling density, therefore, five different structures of internal fillings and two different values of the filling density - 10% and 30% - were prepared using the FDM method. The tested samples were characterised by a large thickness required for a complete formation of selected internal structures. The puncture resistance test process was carried out using a drop hammer. The impact damage was visually assessed. Also, measurements were taken to evaluate the puncture resistance of the tested structures. The obtained results clearly indicate that elements made in 3D printing technology with different internal structures show different resistance to puncture. Among the tested ones, the 3D Honeycomb with 30% structure showed the highest puncture resistance.
***Keywords:*** 3D printing, puncture resistance, filling density.

## 1. INTRODUCTION

Additive manufacturing, referred to as 3D printing, enables a fast and efficient design and manufacture of plastic products. It is an important and progressive element in the area of manufacturing development, [1]. 3D printing is a spatial fabrication process that allows virtual objects - CAD models - to be materialised using layered material application, [2].
3D printing is one of the most modern manufacturing methods. As a production technique, due to the specific nature of creating finished components, it is rather dedicated to single-unit or small-batch manufacturing, [3, 4]. However, due to the widespread availability of relatively inexpensive printing devices and consumables (polymer-based printing), this method has great potential and can be successfully used in many applications. Even now, components made using 3D printing technology are used in automotive [5], aviation [6], medicine [7, 8] and many other fields. It is worth noting that 3D printing allows the manufacture of components with complex external and internal shapes, which, in the case of other manufacturing techniques, often requires advanced equipment and specialised personnel. The creation of components in 3D printing is not burdened by such requirements, which can be used, for example, in field repairs of military equipment, when an emergency repair has to be performed under time pressure and without the availability of the required parts, [9]. Obviously, the polymer part printing technology currently in use has numerous disadvantages, resulting in imperfections in the created objects. Moreover, their mechanical properties can vary when using different printing materials and equipment. Alongside the advancement of 3D printing technology, research efforts are underway to characterise the properties of components produced by this method, as this is crucial for ensuring their safe use. The properties of the printed components depend on many technological factors. Quite frequently, there are difficulties in defining them unambiguously. Experimental research typically focuses on determining the basic static properties of printed materials or components. However, in many real-world structures where these elements are to be applied, they are subjected to varying mechanical loads, including dynamic and impact loads, as well as non-mechanical loads, such as thermal stresses, [10]. The subject explored in the study concerns the puncture resistance of components produced via 3D printing, a significant aspect that is only sporadically addressed in the existing literature. With the growing importance of 3D printing in the aerospace industry, among others, and the wide availability of

choices of fillings and materials to create products, it was decided to investigate how the structure of the inner filling and the density of the filling affect puncture resistance.
One of the 3D printing methods is FDM [11], which involves layer-by-layer deposition of molten material. It is among the most common and versatile additive layer deposition technologies in composite materials. In this technique, the material in the form of a filament from a spool is fed into an extruder, whose task is to deliver the thermoplastic to the print head. There, the filament is heated to its melting temperature, and then the plasticised filament is pushed through the nozzle in the form of a fine thread. It is deposited layer by layer onto the heated bed or onto the previously printed part, depending on the stage of the printing process. A characteristic feature of this method is the necessity of using support structures when the model has a complex geometry. Support structures can be printed in the same material as the entire design or other materials such as PVA, HIPS, or BVOH, whose structure dissolves when immersed in a specialised solution.
Several types of filaments (mainly thermoplastics) can be used in FDM. Each is characterised by distinctive properties that affect both the printing process itself and the characteristics of the resulting product.
The finished component obtained by 3D printing in its simplest form has two structures: outer, in the form of a wall, and an inner one, i.e., an infill. The outer wall can be described as the outer area of the print, the visible part of the object. The accuracy of the execution of this part has a key impact on its visual aspects. In addition, this part protects its interior. However, it is the infill portion of the object that plays a key role in the durability of the design. It affects the entire structure, mass, buoyancy, and strength. Many parameters can be used to model the internal structure of an object; however, the research focused on two fundamental ones: infill density and infill pattern, [12,13].
Density refers to the percentage that expresses the ratio between the volume of the printed filling structure and the total internal volume of the part. An example of a formula with a density range of 0% - 100% is presented in Figure 1.

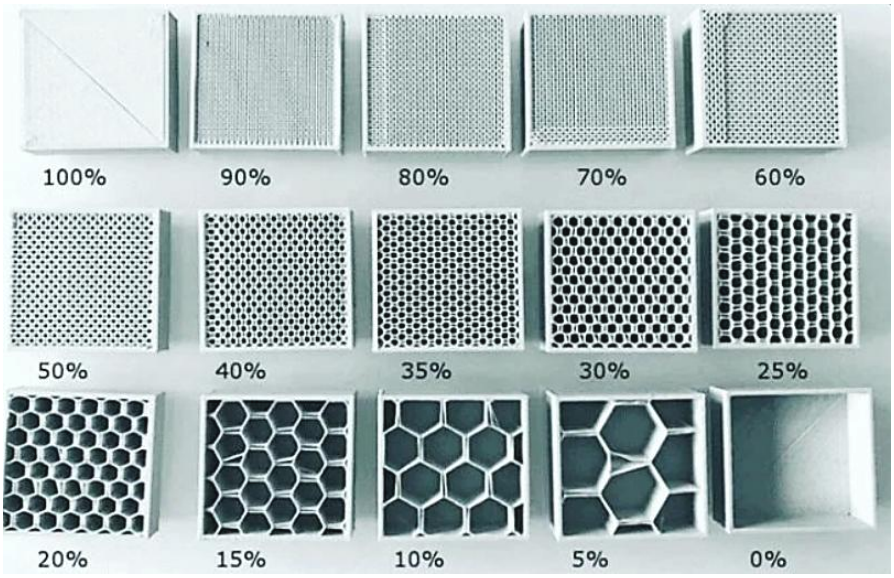

Fig. 1. Different infill density values. Range of density values: 0% - 100%, [14]

In 3D printing, full infill (100% infill density) is rarely used, and completely hollow prints (0% infill density) are rarely created. One of the reasons for not using 100% infill is the high material cost, which is often a decisive factor in the printing process. Another significant factor discouraging the use of full internal infill is the substantially increased weight of the part and the prolonged printing time. Conversely, the use of zero infill is generally avoided due to, among other factors, the insufficient mechanical strength of the resulting parts. A lack of internal infill may also negatively impact the quality of the print, since without sufficient internal support, the upper layers of the model become difficult to print accurately due to gravitational forces and the plastic nature of the material. This can lead to the collapse of the structure and the formation of surface defects caused by the lack of internal stabilization, [12]. In practice, infill densities in the range of 15% to 50% are most commonly used, [13].
The choice of infill shape determines the properties of the product after printing, affecting, among other things, its mechanical properties. The number of available infill designs provides a wide range of possibilities, allowing the user to make an individual choice. Five interior infill designs were selected for the implementation of the study:

• Grid - this is one of the simplest and fastest printed structures. Its pattern consists of a group of parallel lines oriented perpendicularly to each other, forming a mesh of squares (Figure 2a). This structure is classified among the stiffest filling patterns and exhibits exceptionally high stiffness in the vertical axis. The top surface is well supported and thus looks very smooth, [15].

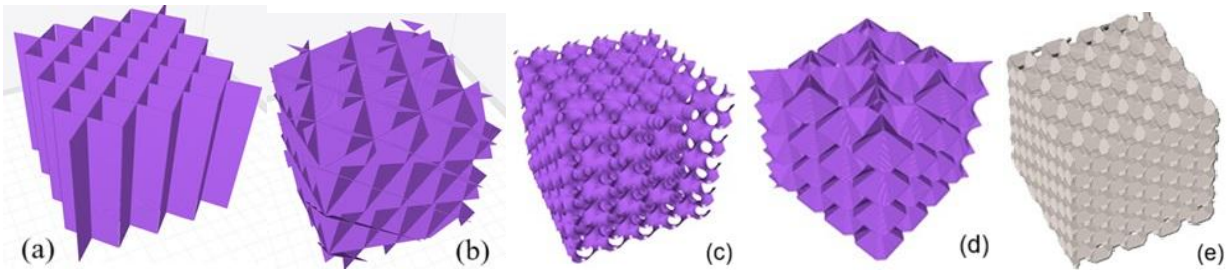

Fig. 2. Form pattern: (a) Grid, (b) Cubic, (c) Gyroid, (d) CROSS 3D, (e) 3D Honeycomb

• Cubic – this type of infill structure is composed of cube-shaped units, with their corners pointing vertically (Figure 2b) It is a formula that ensures the isotropy of the strength, [16].
• Gyroid – a wavy internal infill structure of this type is illustrated in Figure 2c. Its structure provides support for the material in every direction, while being quick to print. Its significant drawback is the lengthy generation of the G-code file, [17].
• Cross 3D - is a cross structure observed in three dimensions (Figure 2d). The internal structure fills the space with intersecting lines that create a cross-like appearance. It creates long yet straight lines that make the filament volume evenly distributed throughout the entire space. It is an impractical pattern due to its low strength in all directions. Due to the complexity of the shape, it also requires a long printing time, [17].
• 3D Honeycomb - a distinctive infill pattern inspired by the honeycomb structure (Figure 2e). The structure appears as a three-dimensional hexagonal mesh, depending on the layer height in the print. This type of structure is an extension of the two-dimensional Honeycomb pattern. When reviewing each layer, it can be seen that they are different from each other and form a series of voids, as in the Cubic pattern. The pattern is used in projects where low weight and high strength are important, [16].

## 2. MATERIALS AND METHODS

The tested objects were samples with varied internal filling structures. In addition to five different internal infill structures of the samples, two different infill density values were selected (10% and 30%).
In order to carry out the planned strength tests, a sample was designed to provide sufficient space for the development of the selected internal infill patterns and to allow for proper testing. All samples were printed on Snapmaker 2.0 A250 and Original Prusa i3 MK3S+ printers using Spectrum Premium PET-G filament, which was chosen as the material to print the samples due to its good mechanical properties (Table 1).

Table 1. Properties of PET-filamentG, [18]

| | |
|---|---|
| Physical properties | |
| Diameter [mm] | 1.75 |
| Density [g/cm$^3$] | 1.38 |
| Thermal properties | |
| Melt flow index [MPa] | 68 |
| Heat Deflection Temperature [°C] | 64 |
| Mechanical properties | |
| Flexural strength [MPa] | 68 |
| Modulus of elasticity in bending [MPa] | 1,800 |
| Tensile strength [MPa] | 49 |
| Impact strength [kJ/m$^2$] | 7.6 |
| Elongation at break [%] | 225 |
| Range of print parameters that can be used | |
| Printing temperature [°C] | 230 – 250 |
| Heated bed temperature [°C] | 60 – 80 |
| Printing speed [mm/s] | 40 – 100 |

The two printers were used to compare their prints, and the SnapMaker printer software did not have the HoneyComb 3D infill. To operate the Prusa printer, we used Prusa Slicer software version 2.8.1 and Luban software version 4.12 for the Snapmaker printer. Basic operating parameters of the used printers with different filaments are presented in Tables 2 and 3.

Table 2. Basic operating parameters of Snapmaker 2.0 A250 3D printer with different filaments, [18]

| Printing parameters | | | | |
|---|---|---|---|---|
| | PLA | ABS | TPU | PET-G |
| Printing temperature [°C] | 190 – 230 | 230 – 240 | 230 – 250 | 230 – 250 |
| Bed temperature [°C] | 45 – 60 | 95 – 110 | 45 – 60 | 60 – 80 |
| Printing speed [$\frac{mm}{s}$] | 40 – 100 | 40 – 100 | 10 – 50 | 40 – 100 |

Table 3. Basic operating parameters of Original Prusa MK3S 3D printer with different filaments, [19]

| Printing parameters | | | | | | | |
|---|---|---|---|---|---|---|---|
| | PLA | ASA/ABS | PET-G | Nylon | PC | Flex | CPE |
| Printing temperature [°C] | 215 | 245 – 265 | 230 – 250 | 240 | 275 | 230 – 260 | 255 – 275 |
| Bed temperature [°C] | 50 – 60 | 90 – 110 | 60 – 80 | 80 – 90 | 110 for the first layer - 115 for the rest of the layers | 45 – 65 | 70 – 90 |

Under the assumed experimental conditions, height was the most critical parameter, as the load was applied in that direction. Using the sample model, it was found that the sample height of less than 20 mm was not possible, due to the fact that the three-dimensional shapes do not achieve sufficient pattern development. On the other hand, increasing the height of the sample beyond the set value of the examination will not affect the test result, as each shape is already fully developed at a height of 20 mm. It was, therefore, assumed that the test samples would be 60x60x20 mm in size.

The criterion for selecting the structures (Cubic, Cross 3D, Grid, Gyroid and 3D Honeycomb) was the strength properties in the thickness direction. Samples with different key parameters were considered, both the ones expected to have high strength in the thickness direction (in the Z-axis direction) and those with lower strength parameters but with other important properties, such as low weight or short print time.

The Grid pattern was selected due to its high Z-axis strength, which is favourable for the expected experimental results. The following structures: Honeycomb 3D and Cubic, which are three-dimensional, provide high strength in every direction and are therefore a valuable choice. The Cross 3D structure is a pattern with unpromising mechanical properties, yet it is characterised by low weight. The Gyroid structure is a pattern suitable for printing objects with medium mechanical strength, as it efficiently distributes applied loads. Nevertheless, due to its porous structure, it lacks high load-bearing capacity. However, like the Cross 3D structure, it enables the production of lightweight prints, [15].

The selected infill densities (10% and 30%) are commonly used in practice, depending on the desired properties for lightweight objects, where low filament consumption is important and strength properties are secondary, a 10% fill is used. A compromise between strength and material consumption is the choice of 30% infill - typical for projects requiring higher strength.

Figures 3 - 7 show the structures of the research objects. These are visualisations of the actual infill for dimensions 60x60x20 mm.

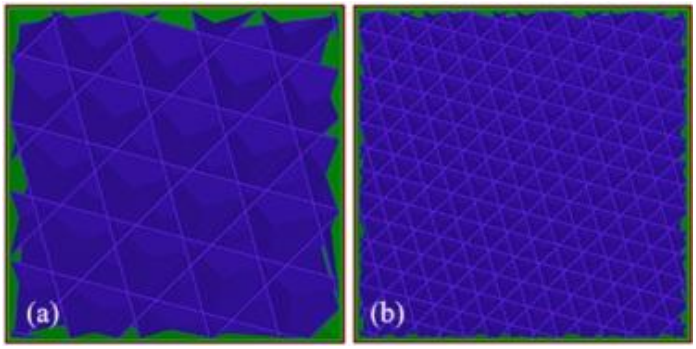


Fig. 3. Structure of the Cubic infill form: (a) 10%, (b) 30% filling density

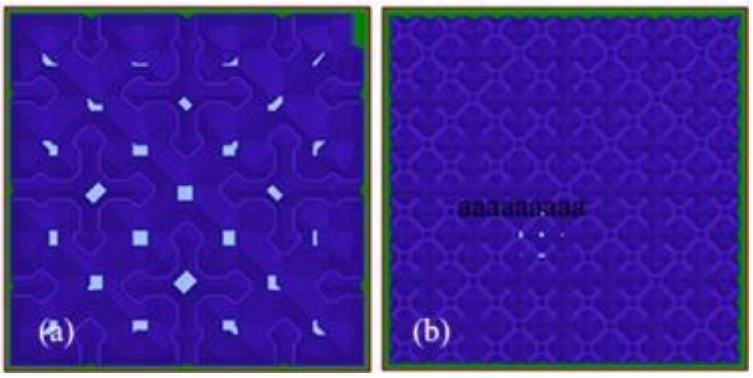

Fig. 4. Structure of the Cross 3D infill form: (a) 10%, (b) 30% filling density

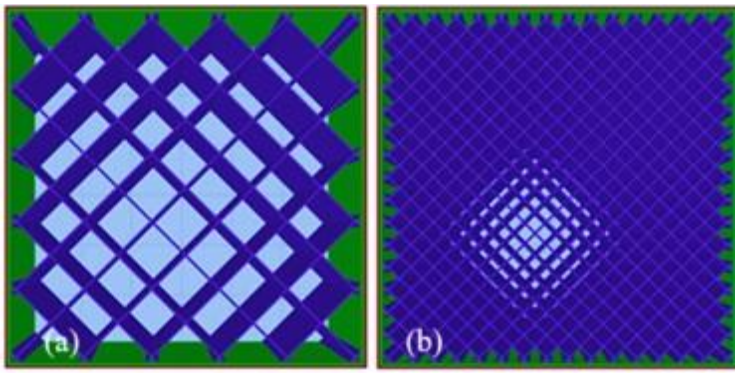

Fig. 5. Structure of the Grid infill form: (a) 10%, (b) 30% filling density

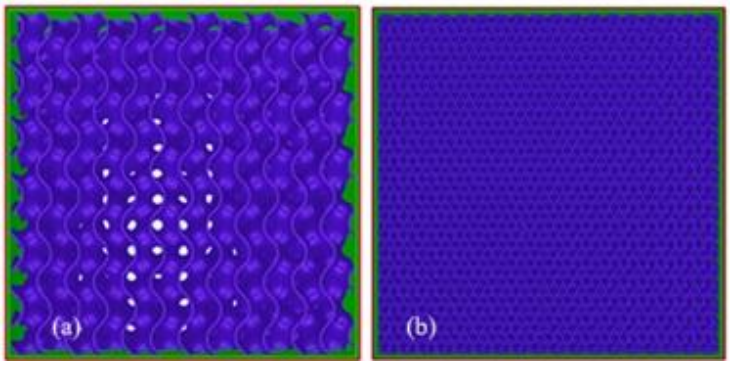

Fig. 6. Structure of the Gyroid infill form: (a) 10%, (b) 30% filling density

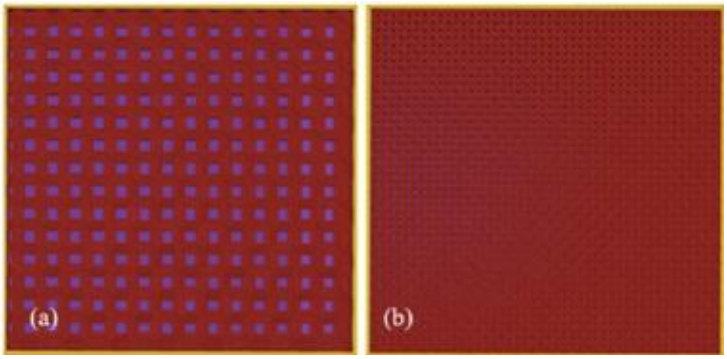

Fig. 7. Structure of the 3D Honeycomb infill form: (a) 10%, (b) 30% filling density

During printing in both printers, we used the same temperatures; the build plate was heated to 75 °C, and the print nozzle operated at 235 °C. A brass nozzle with a diameter of 0.4 mm was used for printing. The printers were set the same: layer height 0.2 mm, bottom thickness 1.2 mm, top thickness 1.2 mm, wall thickness 0.8 mm.
In order to increase the contact area between the print and the build surface, additional filament layers were printed around the model — the so-called 'brim'. This approach is intended to improve adhesion, which reduces the risk of the object detaching from the build plate, minimising material shrinkage. A preview of the initial print settings and the printing process is presented in Figure 8.

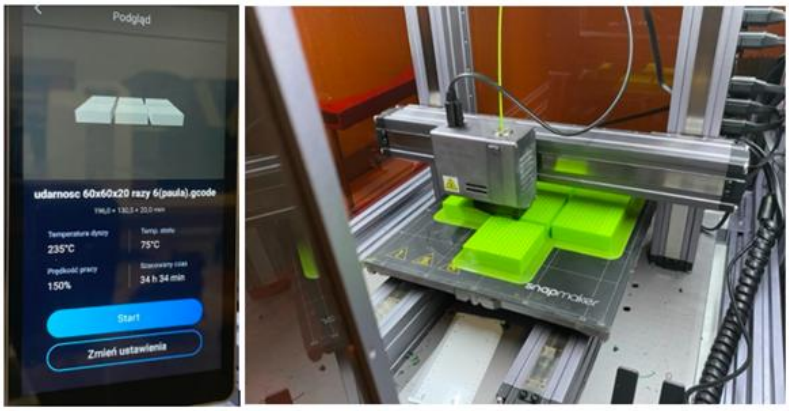

Fig. 8. Preview of initial print settings and print process

After the printing process was completed, the brim layers were manually removed from the printed samples. In field conditions, we often perform repairs under time constraints, we need parts immediately, and to keep the field repair conditions realistic, we did not keep samples at 80-100°C for some time to reduce stresses. The samples (Figure 9) have been described to facilitate their identification. The test batches consisted of five samples in a single infill pattern. Additional samples were used to carry out preliminary tests. It is worth noting that the colours of the filament do not affect the mechanical properties of the materials.

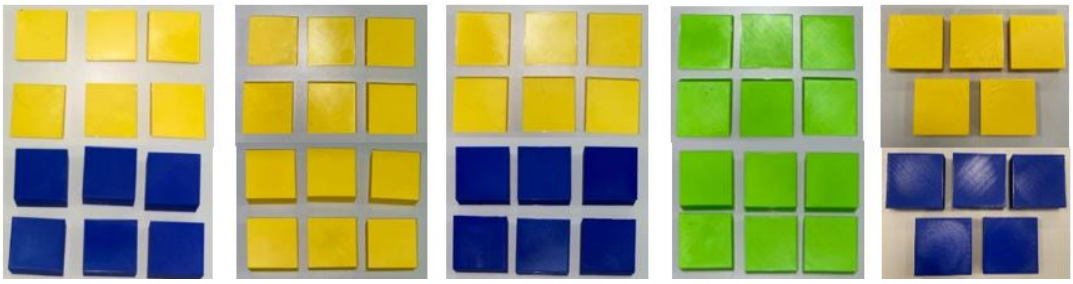
Fig. 9. A set of samples after mechanical treatment

## 3. RESULTS AND DISCUSSIONS

The puncture resistance tests were conducted on an INSTRON CEAST 9340 impact dropping tool. Before conducting the main experiments, their parameters were determined experimentally. In order to establish the energy levels applied in the primary tests, six samples featuring various internal structures were selected. The energy values adopted for the preliminary studies were as follows: 7, 6, 5, and 4 J.

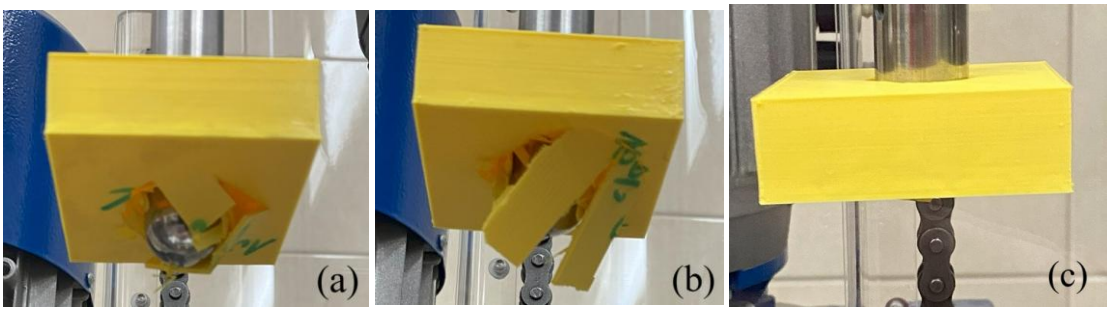

Fig. 10. Damage to samples during preliminary testing. Corresponding drop energy values in sequence: a) 7 J; b) 6 J; c) 5 J

Tests with drop energies of 7, 6, and 5 J resulted in complete penetration of the sample (Figure 10). In view of the promising results obtained at an impact energy of 4 J, this energy level was adopted for the subsequent main tests. A total of 50 tests were performed, in which each sample was loaded once. The tested samples are presented in Figures 11–15.

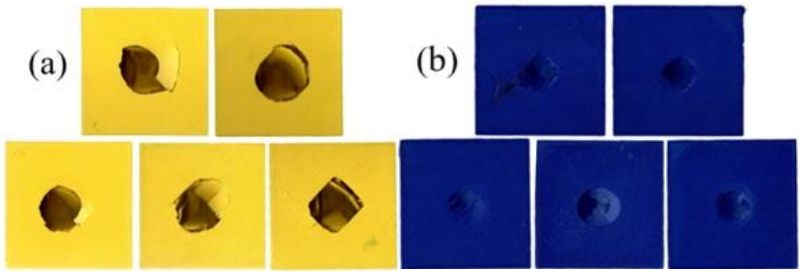

Fig. 11. View of the samples after impact loading with 4 J of energy – Cross 3D structure with the following infill density: (a) 10%, (b) 30%

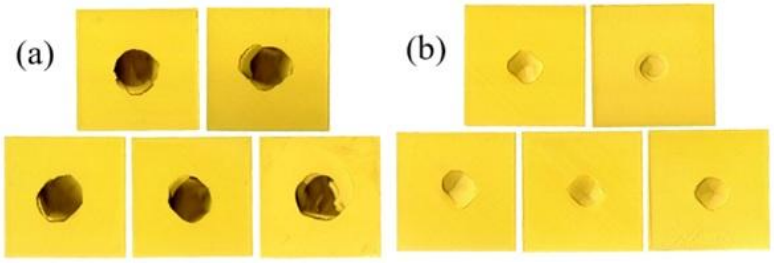

Fig. 12. View of the samples after impact loading with 4 J of energy – Cubic structure with the following infill density: (a) 10%, (b) 30%

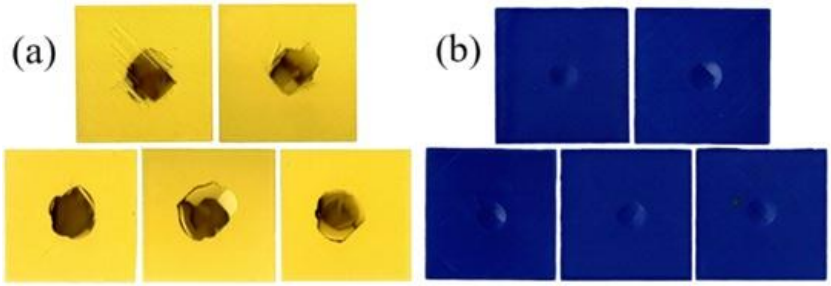

Fig. 13. View of the samples after impact loading with 4 J of energy – Grid structure with the following infill density: (a) 10%, (b) 30%

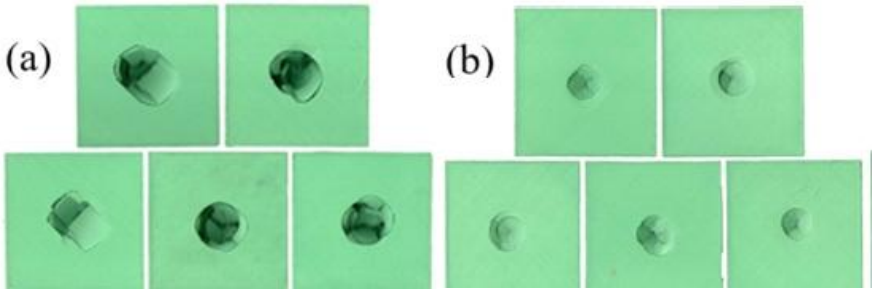

Fig. 14. View of the samples after impact loading with 4 J of energy – Gyroid structure with the following infill density: (a) 10%, (b) 30%

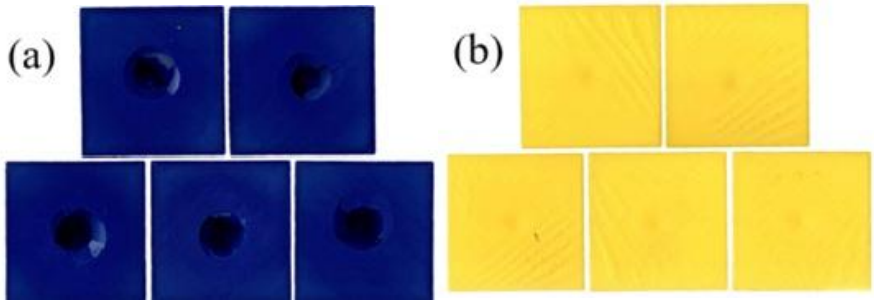

Fig. 15. View of the samples after impact loading with 4 J of energy – 3d Honeycomb structure with the following infill density: (a) 10%, (b) 30%

The assessment of the puncture resistance of the printed structures was based on measuring the penetration depth parameters of the impactor into the tested object (Figure 16). The damage depth values were measured using an indirect method with a dial gauge indicator measuring depth (Figure 17).


Fig. 16. Measurement of the penetration depth in the examined object using a dial gauge indicator

It was also decided to carry out a visual analysis of the damage to the internal structure of the samples by observing their cross-sections along the diagonal (Figure 18), as depicted in Figures 19 - 21.

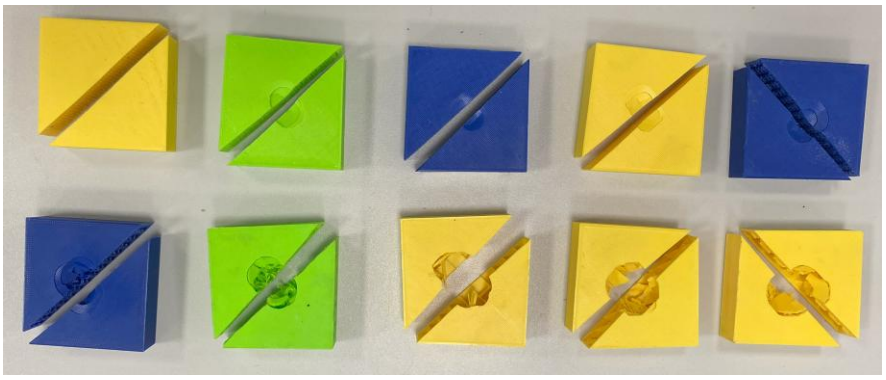

Fig. 17. Cross-sections of the tested samples

The internal structure of the Gyroid sample with 30% infill density (Figure 18a) reveals internal damage after sectioning (plastic deformation of the internal structure to a depth of 3 mm beneath the area of surface layer deformation, without cracking), which was not visible during the surface inspection prior to cutting the sample. At an infill density of 10% (Figure 18b), significant damage can be observed in the direction of the applied load, manifested as deformation of the internal structure extending to the bottom of the sample, accompanied by visible fractures in structural elements.

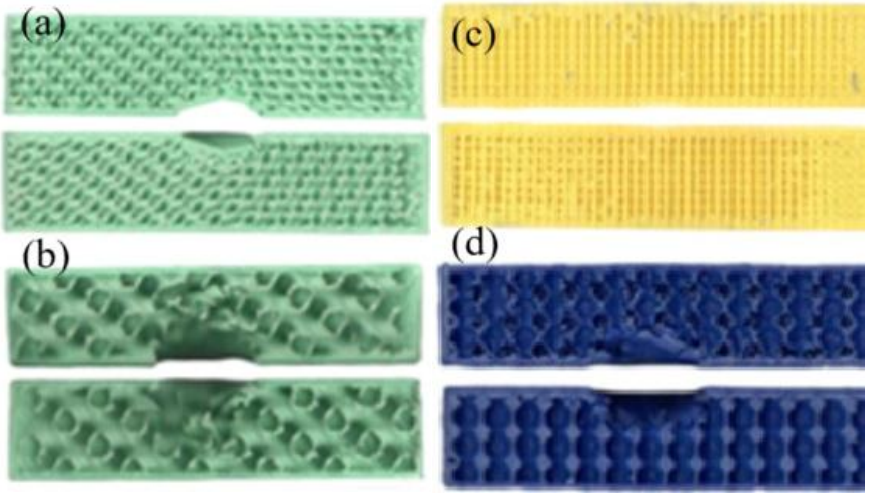


Fig. 18. Cross-section of a sample with the following structure: Gyroid (a) 30, (b) Gyroid 10%, (c) 3D Honeycomb 30%, (d) 3D Honeycomb 10%

The 3D Honeycomb sample with 10% infill (Figure 18c), despite evident surface damage, does not exhibit internal damage exceeding the nature and extent of the surface defects. No internal damage was observed in the 3D Honeycomb sample with 30% infill density (Figure 18d).

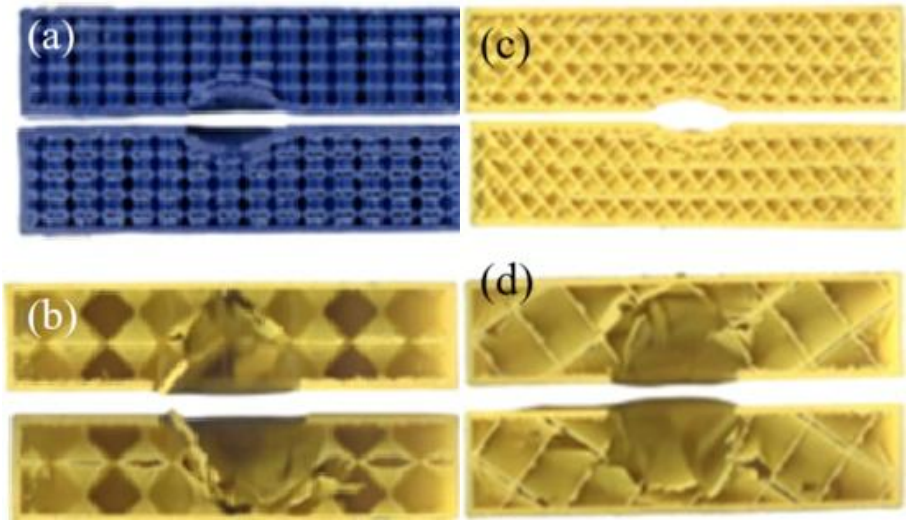


Fig. 19. Cross-section of a sample with the following structure: (a) Cubic 30%, (b) Cubic 10%, (c)Cross 3D 30%, (d) Cross 3D 10%

The internal Cubic structure with a 30% infill density (Figure 19a) reveals deformation of one layer located directly beneath the surface damage. The other layers in the direction of load application are not damaged. In the Cubic structure with 10% infill (Figure 19b), the top layer was penetrated, and the cross-section reveals extensive internal damage reaching the base of the sample and the cells adjacent to the damaged area.
In the Cross 3D sample with 30% infill density (Figure 19c), internal damage is visible, consisting of plastic deformation and cracking in the layer beneath the point of load application. The Cross structure with 10% infill (Figure 19d) shows, in cross-section, severe damage resulting from the penetration of the top layer. The damage reaches the base of the sample and impacts the cells bordering the affected region. Significant losses in the internal structure are visible.

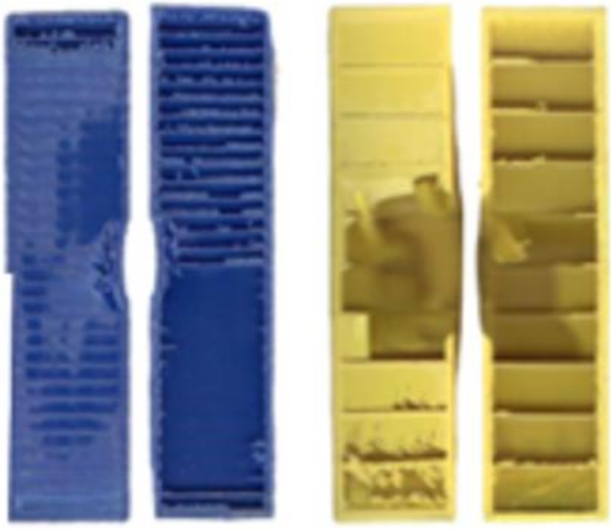

Fig. 20. Cross-section of the sample with Grid structure: (a) 30%, (b) 10%

The Grid sample with 30% infill density (Figure 20a) in cross-section, reveals plastic deformations extending to a depth of 3 mm beneath the surface layer. No internal damage was observed outside the load application area. The Grid 10% structure (Figure 20b) shows significant loss and damage after cutting, extending to the base of the sample.
Based on the results presented in Table 4, a chart was created showing the ratio of damage depth to sample height (Figure 21), which illustrates the relative size of the damage in the vertical direction.

Table 4. The ratio of the sample's damage depth to its height

| Infill shape | *Infill density [%]* | *The ratio of the sample's damage depth to its height [%]* |
|---|---|---|
| Cross 3D | 10 | 92.86±0.05 |
| | 30 | 18.75±0.46 |
| Cubic | 10 | 86.63±1.33 |
| | 30 | 14.49±0.37 |
| Grid | 10 | 92.76±0.05 |
| | 30 | 4.76±0.29 |
| Gyroid | 10 | 45.05±2.42 |
| | 30 | 16.56±0.38 |
| 3D Honeycomb | 10 | 40.68±0.05 |
| | 30 | 0.84±0.04 |

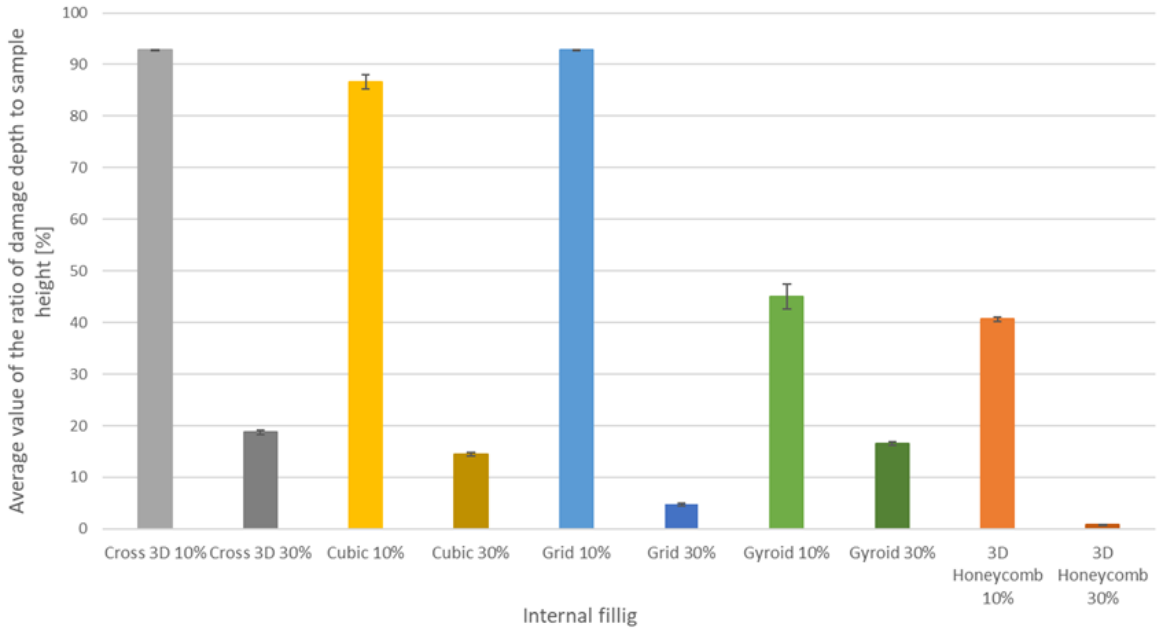


Fig. 21. The ratio of the sample's damage depth to its height expressed as a percentage

In each case, it was observed that an increase in internal infill density results in increased puncture resistance. The 3D Honeycomb structure with 30% infill demonstrated the highest resistance among the tested configurations, with an average damage depth-to-sample height ratio of 0.84%. The Grid 30% structure, which was the only two-dimensional internal infill, also exhibited a low damage depth-to-sample height ratio of 4.76% It can be concluded that the response of the internal infill to sudden loading does not depend on its spatial complexity. The infill structures that proved to be the least resistant during the impact test were also identified: Cross 3D 10%, Cubic 10% and Grid 10%. Their internal structure was almost destroyed, exceeding more than 85% of the damage value in the axis along which the impact load was applied. Of the infills with 10% infill density, the best results were obtained for the samples: Gyroid 10% – 45.05% and 3D Honeycomb 10% – 40.68%, which suggests that they are suitable options among infill structures designed for low-mass applications.

A significant scatter in the results was observed for the following structures: Cubic 10% and Gyroid 10%. The remaining infill structures are characterised by a low scatter of the results, ensuring data uniformity, which makes them predictable infill types.

The average damage depth of the samples presented in Figure 23 does not fully reflect the range of results obtained in each series. The damage depth values showed significant variation depending on the internal structure. Therefore, it was additionally decided to present a graphical representation of the sample depth values, including the range between the minimum and maximum recorded results. The graph shown in Figure 22 is to emphasise that the extent of damage was influenced by the structural uniformity and also identifies infill configurations that exhibited high result consistency. The Y-axis, labelled from 0 to 20 mm, is oriented downward, corresponding to the height of the sample and the direction of the conducted test.

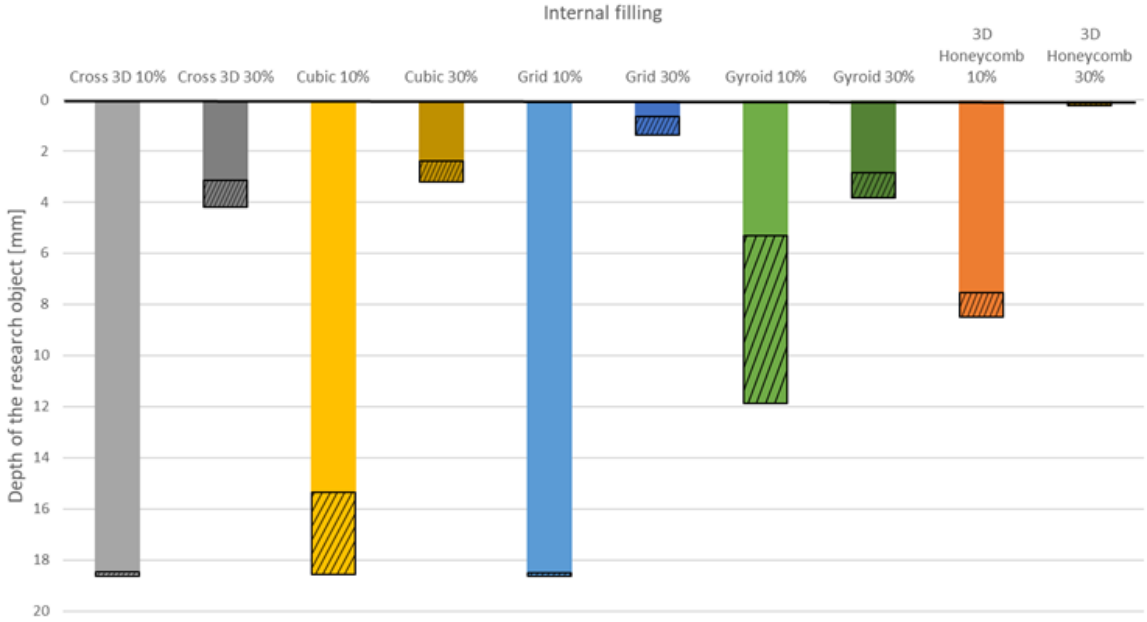


Key:
- Depth of damage obtained for each sample.
- Range between the smallest and the largest depth of damage.

Fig. 22. Damage depth value of tested samples

In batch series: Cross 3D 10%, Grid 10%, 3D Honeycomb 10%, a slight discrepancy in results was observed, indicating a high degree of structural homogeneity. For the infills where the damage reached the greatest depth, the deviation of the results may have been influenced by the presence of the last, thicker outer wall layer. A large discrepancy in results can be seen in the series of samples: Cubic 10% and Gyroid 10%. The obtained results may suggest that the structures are heterogeneous.
The 3D Honeycomb structure surface with an infill density of 30% was the only one that was not interrupted and has the smallest scatter between results in the test series, making it the most reliable in terms of quality of results. No clear relationship was observed between the value of filling density and the scatter of results.
The damage visible on the top surface of the samples, perpendicular to which the load was applied, was then analysed.
The analysis of the damaged area on the top wall was conducted using the ImageJ software, which was employed to process the imported image. The application made it possible to measure the area of the indentation created by the impact load. In order to minimise the measurement error, the damaged surface area of each sample was measured three times.

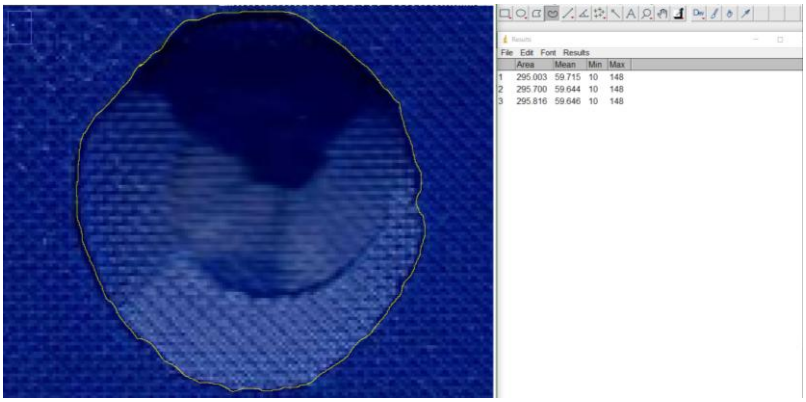

Fig. 23. Measurement of damage to the outer surface of an example test object with three indentation field results

When determining the area of the damaged surface structure of the sample, surrounding post-impact deformations, such as slight material distortions, were also taken into account (Figure 23).
Based on the collected data (Table 5), a graph was prepared (Figure 24) showing the average surface area of the indentation in the samples.

Table 5. Average post-impact indentation surface area values

| Infill shape | Infill density [%] | The ratio of the sample's damage depth to its height [%] |
|---|---|---|
| Cross 3D | 10 | 458.51±66.86 |
| | 30 | 247.01±44.61 |
| Cubic | 10 | 426.92±71.73 |
| | 30 | 235.06±35.00 |
| Grid | 10 | 461.33±101.19 |
| | 30 | 140.63±11.73 |
| Gyroid | 10 | 418.60±55.36 |
| | 30 | 213.73±46.55 |
| 3D Honeycomb | 10 | 446.04±53.54 |
| | 30 | 42.05±2.71 |

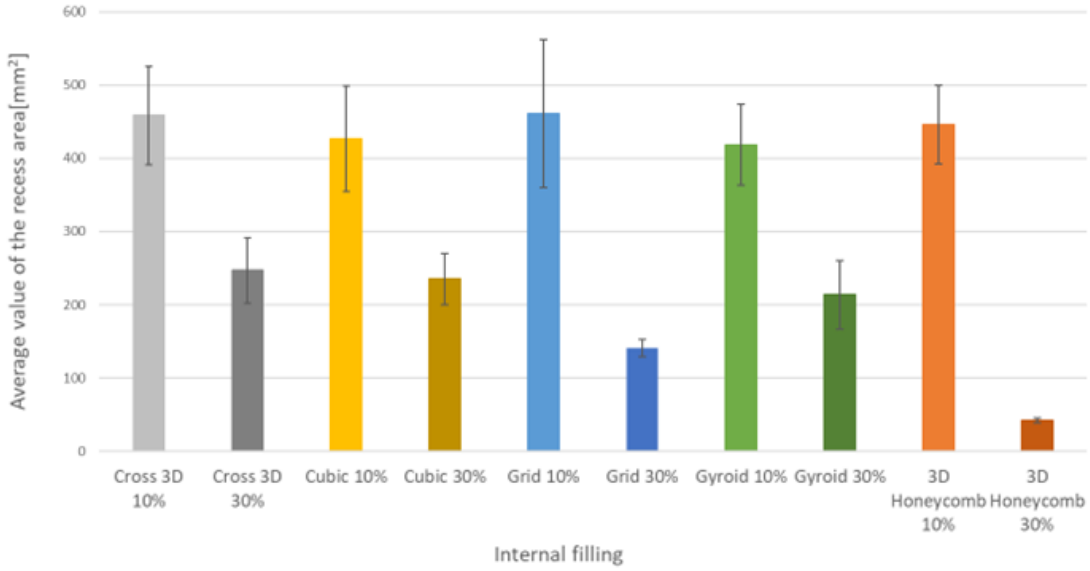


Fig. 24. Average post-impact indentation surface area values

It was observed that the 30% Honeycomb 3D structure exhibited the smallest post-impact indentation area (plastic deformation). Its average value is 42.05 mm$^2$, which means that the damage represents just over 1% of the area of the impacted wall. Another structure that demonstrated high resistance was the 30% Grid, with an average indentation area of 140.63 mm$^2$. This may indicate that a portion of the impact energy was absorbed by the internal structure. Observation of the 3D Honeycomb 30% samples also showed no surface cracks. This is a very important observation as it suggests good elastic properties of the structure and good resistance to dynamic loading. Samples with internal infill characterised by 30% density exhibited the lowest deformation area, indicating an increase in dynamic strength proportional to the infill density. The variants with 10% infill density showed a failure area in the range 410 - 460 mm$^2$, with an average of 442.28 mm$^2$.

Each object with a unique internal structure is characterised by certain properties that result in differences in printing time. Figure 25 and Figure 26 show the relationships of selected physical properties of the tested materials. In order to print 50 samples, 1,336 grams of PET-G filament were used, and the total printing time amounted to 161.02 hours.

When analysing the results (Figure 25), it can be observed that the highest values for mass and manufacture time are characterised by the 3D Honeycomb 30% sample series, with a mass of 220 g and a printed time of 20.80 h. Among the tested variants, the Cubic 10% sample series exhibited the lowest mass at 93 g, whereas the 3D Honeycomb 10% samples achieved the shortest printing time of 9.18 hours.

It is worth noting the concentration of data in specific areas of the graph. The following infills: Cross 3D 10%, Cubic 10%, Grid 10%, and Gyroid 10% are clustered, which may indicate that, while exhibiting similar characteristics, they are comparable in terms of properties. The same phenomenon was observed for samples with the following infills: Cross 3D 30%, Cubic 30%, Grid 30%, Gyroid 30%. The Gyroid 30% structure shows a slight deviation from the other grouped elements, being characterised by a lower mass. It should be noted that the observed data concentrations pertain to samples with identical internal infill density. The 3D Honeycomb 10% and 30% structures appear to be unrelated to the features observed in the other pattern groups. The reason for this may be the use of a different 3D printer (Original Prusa MK3S+) to produce the 3D Honeycomb structured pattern objects, and a different 3D printer (Snapmaker 2.0 A250) to produce the other components. A correlation was

also identified, indicating that the mass of the element increases proportionally with the amount of material used for its production.

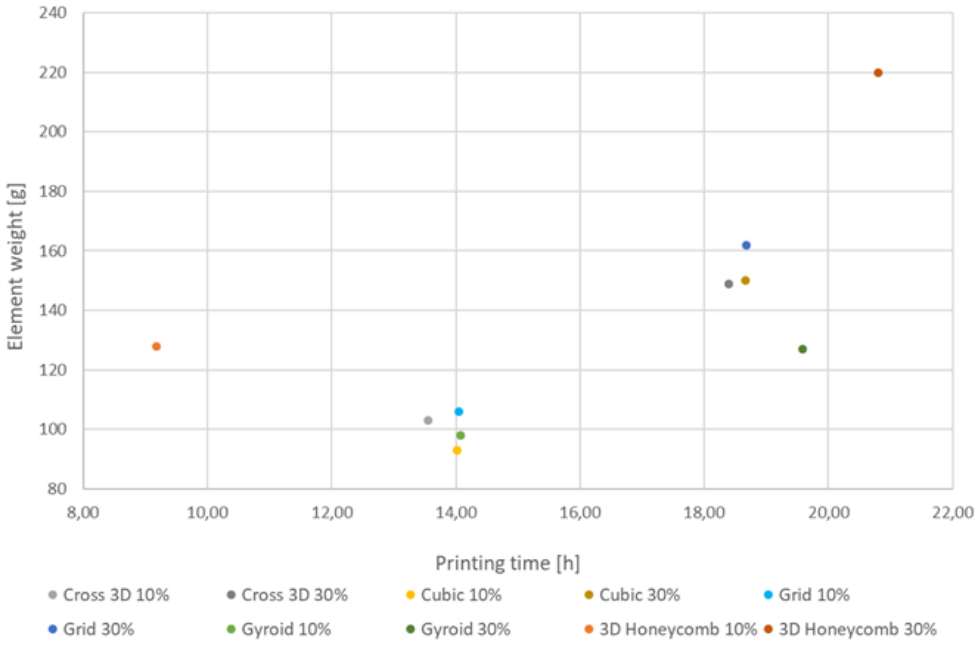


Fig. 25. Characteristics of the test sample mass as a function of printing time

In addition, the ratio of sample weight to printing time was calculated from the collected data and is shown in Figure 26. The ratio of mass to printing time of the components created by 3D printing makes it possible to identify the structure that, with the highest mass, requires the shortest printing time.

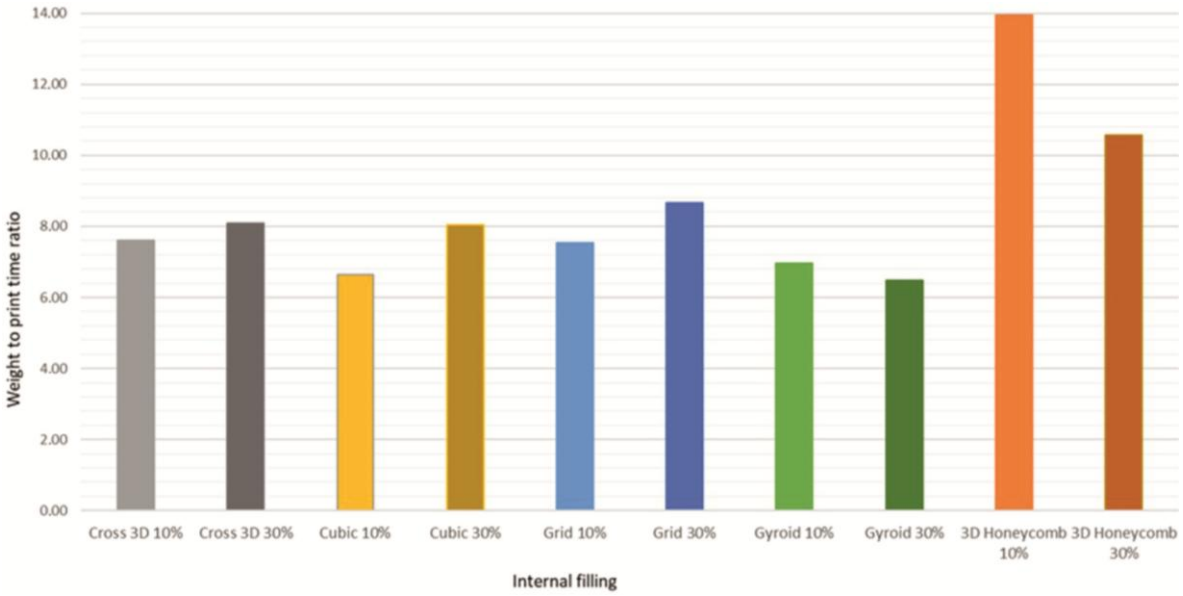


Fig. 26. Ratio of sample mass to printing time

Upon examining the graph (Figure 26), considerable distinctions can be observed between the 3D Honeycomb structure and the remaining infill patterns. The 3D Honeycomb structure is characterised by significantly higher values of the mass-to-printing-time ratio, indicating that it is the most efficient structure among those studied in terms of 3D printing performance. The highest weight-to-print time ratio was achieved with 3D Honeycomb 10% infill, where a print speed of 13.94 g/h could be achieved. It was also noted that for parts made with the Snapmaker 2.0 A250 3D printer, the difference between structures with 10 % and 30 % infill is not clear. Most values are in the 6 - 8 g/h range with three structures outside this range: Cross 3D 30% for which the ratio is 8.10 g/h, Cubic 30% for which the ratio is 8.04 g/h, and Grid 30% for which the ratio is 8.67 g/h. The lowest results were for structures: Cubic 10% and Gyroid 30%, for which the ratio values were 6.63 g/h and 6.49 g/h, respectively, suggesting that they are not good patterns for printing if large amounts of material are used.

## 4. CONCLUSIONS

The obtained results clearly indicate that 3D printed components with different internal structures show different puncture resistance. The 3D Honeycomb 30% structure proved to be the most effective among the tested variants, achieving the lowest post-impact indentation value of 0.17 in the examined sample. mm Additionally, the 3D Honeycomb structure also showed the smallest post-impact indentation surface area in the sample.
It appears that an infill density of 10 % cannot be used for printing components exposed to even low-energy impact loads during operation.
In some of the tested samples, the outer layer was punctured, which, given the applied infill densities, caused significant damage to their internal structures. In samples where the surface layer was not punctured, small fragments of the inner fillings underwent plastic deformation.
Further studies should include residual strength testing of samples whose outer layers remained intact, as well as testing of samples prepared from materials with lower Young's modulus, which could influence the puncture resistance of the printed components.

**Author contributions:** conceptualization (conception or design of the paper) P.M, A.K.; data curation (acquisition/analysis/data interpretation) P.M.; investigation P.M., R.B., A.K.; methodology A.K. R.B.; project administration A.K.; resources P.M, R.B.; software (creation of new software used in the paper) P.M.; supervision A.K.; validation P.M., A.K.; visualization P.M, A.K. R.B. J.K.; initial draft writing P.M., A.K.; review and editing A.K, J.K., M.M.; funding acquisition R.B.
**Funding source**: This paper has received no external funding.
**Conflicts of interest:** There is no conflict of interest.

## 5. REFERENCES

[1]. Boon W., van Wee B. (2018) *Influence of 3D printing on transport: a theory and experts judgment based conceptual model*, Transport Reviews, 38:5, 556-575, DOI: 10.1080/01441647.2017.1370036
[2]. Dudek P. (2013). *FDM 3D Printing Technology in Manufacturing Composite Elements*. Archives of Metallurgy and Materials. 58(4):1415-1418, DOI:10.2478/amm-2013-0186
[3]. Ali M.H., Yerbolat G., Amangeldi S. (2018) *Material Optimization Method in 3D Printing*, 2018 IEEE International Conference on Advanced Manufacturing (ICAM), Yunlin, Taiwan, 365-368, doi: 10.1109/AMCON.2018.8614886.
[4]. Jordan J.M. (2019), 3D Printing. MIT Press, USA.
[5]. Tuazon B.J., Custodio N.A.V., Basuel R.B., Delos Reyes L.A., Dizon J. R.C. (2022). *3D printing technology and materials for automotive application: a mini-review*. Key Engineering Materials, 913, 3-16.
[6]. Martinez D.W., Espino M.T., Cascolan H.M., Crisostomo J.L., Dizon J.R.C. (2022). *A comprehensive review on the application of 3D printing in the aerospace industry*. Key engineering materials, 913, 27-34.
[7]. Ballard D.H., Trace A.P., Ali S., Hodgdon T., Zygmont M.E., DeBenedectis C.M., Lenchik L. (2018). *Clinical applications of 3D printing: primer for radiologists.* Academic radiology, 25(1), 52-65.
[8]. Nadagouda M.N., Rastogi V., Ginn M. (2020). *A review on 3D printing techniques for medical applications*. Current Opinion in Chemical Engineering, 28, 152-157.
[9]. Park M. (2017). *Print to repair: 3D printing and product repair.* In Routledge Handbook of Sustainable Product Design (pp. 236-249). Routledge.
[10]. Grasso M., Azzouz L., Ruiz-Hincapie P., Zarrelli M., Ren G. (2018). *Effect of temperature on the mechanical properties of 3D-printed PLA tensile specimens*. Rapid Prototyping Journal, 24(8), 1337-1346
[11]. Marșavina L., Vălean C., Mărghitaș M., Linul E., Razavi N., Berto F., Brighenti R. (2022). *Effect of the manufacturing parameters on the tensile and fracture properties of FDM 3D-printed PLA specimens*. Engineering Fracture Mechanics, 274, 108766.
[12]. Johnson G., French J. (2018), *Evaluation of Infill Effect on Mechanical Properties of Consumer Printing Materials*, Advances in Technology Innovation 3 (4), 179-84.
[13]. Palinkas I, Desnica E, Pekez J, Letic D. (2022) *Types and Application of Infill in FDM Printing: Review*. Acta Technica Corviniensis - Bulletin of Engineering. 15(2), 55–8
[14]. Infill structure, https://www.cytron.io/tutorial/a-simple-guide-to-infill-in-3d-printing (access date 13.01.2025)
[15]. Buj-Corral I., Bagheri A., Domínguez-Fernández A., Casado-López, R. (2019). *Influence of infill and nozzle diameter on porosity of FDM printed parts with rectilinear grid pattern*. Procedia Manufacturing, 41, 288-295.

[16]. Tanveer M.Q., Mishra G., Mishra S., Sharma, R. (2022). *Effect of infill pattern and infill density on mechanical behaviour of FDM 3D printed Parts-a current review*. Materials Today: Proceedings, 62, 100-108.
[17]. Bacak S., Özkavak H.V., Sofu M.M. (2021). *Comparison of Mechanical Properties of 3D-Printed Specimens Manufactured Via FDM with Various Inner Geometries*. Journal of the Institute of Science and Technology, 11(2), 1444-1454.
[18]. User Manual, Snapmaker, https://s3.us-west-2.amazonaws.com/snapmaker.com/download/manual/Snapmaker2_User_Manual_EN_V1.1.0.pdf (access date 13.01.2025)
[19]. Podręcznik Drukowania 3D, Prusa Reaserch, wersja 3.17, 2021 https://help.prusa3d.com/pl/article/podreczniki-druku_125045 (access date 13.01.2025)

Received: March 15th, 2026 / Accepted: June 15th, 2026 / Paper available online: June 20th, 2026 